agriculture

Article

Remotely Sensed Prediction of Rice Yield at Different Growth Durations Using UAV Multispectral Imagery

Shanjun Luo [1], Xueqin Jiang [2,*], Weihua Jiao [3], Kaili Yang [1], Yuanjin Li [1] and Shenghui Fang [1,*]

[1] School of Remote Sensing and Information Engineering, Wuhan University, Wuhan 430079, China
[2] School of Information Science and Engineering, Shandong Agriculture University, Tai'an 271001, China
[3] Center for Agricultural and Rural Economic Research, Shandong University of Finance and Economics, Jinan 250014, China
* Correspondence: xueqinjiang@whu.edu.cn (X.J.); shfang@whu.edu.cn (S.F.)

Abstract: A precise forecast of rice yields at the plot scale is essential for both food security and precision agriculture. In this work, we developed a novel technique to integrate UAV-based vegetation indices (VIs) with brightness, greenness, and moisture information obtained via tasseled cap transformation (TCT) to improve the precision of rice-yield estimates and eliminate saturation. Eight nitrogen gradients of rice were cultivated to acquire measurements on the ground, as well as six-band UAV images during the booting and heading periods. Several plot-level VIs were then computed based on the canopy reflectance derived from the UAV images. Meanwhile, the TCT-based retrieval of the plot brightness (B), greenness (G), and a third component (T) indicating the state of the rice growing and environmental information, was performed. The findings indicate that ground measurements are solely applicable to estimating rice yields at the booting stage. Furthermore, the VIs in conjunction with the TCT parameters exhibited a greater ability to predict the rice yields than the VIs alone. The final simulation models showed the highest accuracy at the booting stage, but with varying degrees of saturation. The yield-prediction models at the heading stage satisfied the requirement of high precision, without any obvious saturation phenomenon. The product of the VIs and the difference between the T and G (T − G) and the quotient of the T and B (T/B) was the optimum parameter for predicting the rice yield at the heading stage, with an estimation error below 7%. This study offers a guide and reference for rice-yield estimation and precision agriculture.

Keywords: yield estimation; rice; unmanned aerial vehicle (UAV); tasseled cap transformation; precision agriculture

check for updates

Citation: Luo, S.; Jiang, X.; Jiao, W.; Yang, K.; Li, Y.; Fang, S. Remotely Sensed Prediction of Rice Yield at Different Growth Durations Using UAV Multispectral Imagery. *Agriculture* **2022**, *12*, 1447. https://doi.org/10.3390/agriculture12091447

Academic Editors: Jibo Yue, Chengquan Zhou, Haikuan Feng, Yanjun Yang and Ning Zhang

Received: 10 August 2022
Accepted: 9 September 2022
Published: 13 September 2022

1. Introduction

As the largest grain crop in the world and a staple food for over half of the global population, the research on rice is of crucial importance for agricultural systems and food production [1]. Rice-yield data are vital reference indicators for species selection and breeding, determined by the combination of genes and the growth environment. The accurate prediction of rice yields, and especially at the regional level, is of great relevance to guaranteeing food security and sustainable agricultural development, and it is concerned with the elaboration of major policies for national livelihoods [2].

The conventional methods for crop-yield estimates include field sampling [3] and the crop-growth model [4]. The field survey is a devastating assessment method. Although the accuracy of the results can be maintained through a comprehensive investigation, it is undoubtedly a laborious and lengthy task [5]. Crop-growth models incorporate multiple data sources and approaches, which greatly compound their complexity due to the many model input parameters [6]. The remote estimation of yields is a technology that can be used to develop a connection between crop spectra and yield data. Remote sensing (RS) provides a convenient way to efficiently acquire spectral data of vegetation canopies in a nondestructive manner, which carries considerable valuable information regarding the interaction between the canopy and solar radiation, such as the vegetation absorption and scattering [7]. Vegetation-canopy spectra are intimately associated with crop growth, and especially in the visible ranges affected by pigmentation and the near-infrared (NIR) bands subject to the cell tissue and canopy structure [8]. Therefore, the vegetation indices (VIs) derived from these bands have been frequently adopted to estimate the vegetation phenotypic parameters, such as the leaf-area index (LAI), biomass, chlorophyll content, and nitrogen content [9,10]. In general, remote estimates of crop yields using VI-based methods have become mainstream [11].

As for the data source, it is an influential factor in crop-yield estimations. Yield estimations using ground-based measurement spectra are hardly adequate for large areas, and the real-time forecasting requirements and performance are regionally limited [12]. Satellite imagery can be appropriate and cost-effective data for crop monitoring at the regional scale [13]. However, cloud coverage is pervasive during the pivotal crop-growing season, and thus, sufficient spatial- and temporal-resolution data may not be available for precision agriculture. The emergence and development of unmanned aerial vehicles (UAVs) and lightweight sensors can be complementary between satellites and ground-based sensors [14]. Because UAVs have easy access to dynamic data, they have enormous potential to solve and refine strategies for the challenges encountered in agriculture. Despite some shortcomings, such as the flight time, load capacity, and weather situation, UAVs are expected to be applied with high frequency in agriculture from now on due to the valued information gained and effective implementation [15]. The spectral information gained from UAV-based multispectral or hyperspectral data has been broadly applied for crop-growth monitoring and parameter estimation [16]. Moreover, multispectral images, free from the information redundancy and complicated processing of hyperspectral data, have a red-edge band that RGB digital images lack, and their centimeter-level spatial resolutions make multispectral sensors preferred devices in precision agriculture [17].

The reproductive stages of rice can be divided into the tillering, jointing, booting, heading, filling, and maturity stages. During the booting and heading stages, the rice plant progressively accomplishes the conversion from nutritional to reproductive growth, and the appropriate parameters for the yield estimation differ at different stages [18]. In practical terms, it is imperative to access early and precise rice-yield data prior to harvest for market decisions and policymaking. In the early stages of rice growth, the leaves are not yet fully grown, and the variations in the later growth process make it difficult to estimate the yield accurately. However, it may be too late to use data collected at the later stages for yield estimation, as some effective measures need to be scheduled in advance. Moreover, the appearance of rice spikes during mid-to-late growth can interfere with the spectral characteristics of rice, as the color of the spikes eventually turns yellow, causing the overall spectral pattern of the rice to deviate from the normal green vegetation. Zhou et al. revealed that the presence of spikes increased the challenge of yield prediction in the late reproductive stage of rice [19]. Duan et al. also noted that the reduced predictive ability during the heading stage may be related to the uneven penetration of spikes into the sensor field [20]. Hence, the booting and heading stages are suitable for rice-yield estimation, but the heading stage needs to overcome the effect of the spikes.

The tasseled cap transformation (TCT), a viable pioneer of feature-detection algorithms, is a linear-conversion technique that is commonly utilized in the areas of vegetation, soil, and land-cover mapping [21]. The vast majority of the variations in the spectra of a single scene can be interpreted in terms of the brightness, greenness, and humidity retrieved from TCT [22]. Therefore, TCT was exploited to extract the brightness, greenness, and moisture components of the rice fields to provide potentially valuable variables for yield estimation.

In our experiment, the canopy spectral data of the paddy field was remotely measured from both the ground and UAV-mounted platforms, which had quite high spatial resolution, and thus, well-reflecting variations of field. Meanwhile, the LAI and chlorophyll-content data (SPAD) in the same period were obtained. Unlike previous studies, we compared the yield-estimation performance of the ground and UAV-based parameters at different periods, and we combined the TCT parameters to improve the accuracy of the rice-yield estimation without saturation. With rice grown under different nitrogen-fertilizer treatments, our objectives were: (1) to compare the ability of the rice-yield estimation at the booting and heading stages; (2) to accurately estimate the rice yield by ground measurements and UAV data; (3) to explore improving the VI-based approach for rice-yield estimation by integrating the brightness, greenness, and wetness retrieval from TCT.

2. Materials and Methods

2.1. Study Area and Experimental Design

The study area was located in Wuxue City, Hubei Province, China (Figure 1a). It has a humid subtropical monsoon climate with long plant production cycles and abundant rainfall. It is suitable for the comprehensive development of agriculture, forestry, animal husbandry, and fishing. As shown in Figure 1b, the identical rice variety was cultivated in 24 plots with different N-fertilizer-application levels, with a whole area of about 480 m^2 and a total of 7920 rice plants. The ridges between each plot were covered with white plastic film to isolate the mixing of water in the field. There were eight N-fertilizer gradients, and three replications, applying N_0, N_3, $N_{5.5}$, $N_{8.5}$, N_{11}, N_{14}, $N_{16.5}$, and $N_{19.5}$ (unit: kg/ha). Two important growth periods (the booting and heading stages) were selected for the UAV flight experiments. In the former period, no spikes appeared, and in the later period, almost all spikes were clearly present. The conditions were strictly identically controlled, except for differences in the amount of the nitrogen-fertilizer application. Field maintenance, including weeding and pest control, was performed by professionals throughout the growing season.

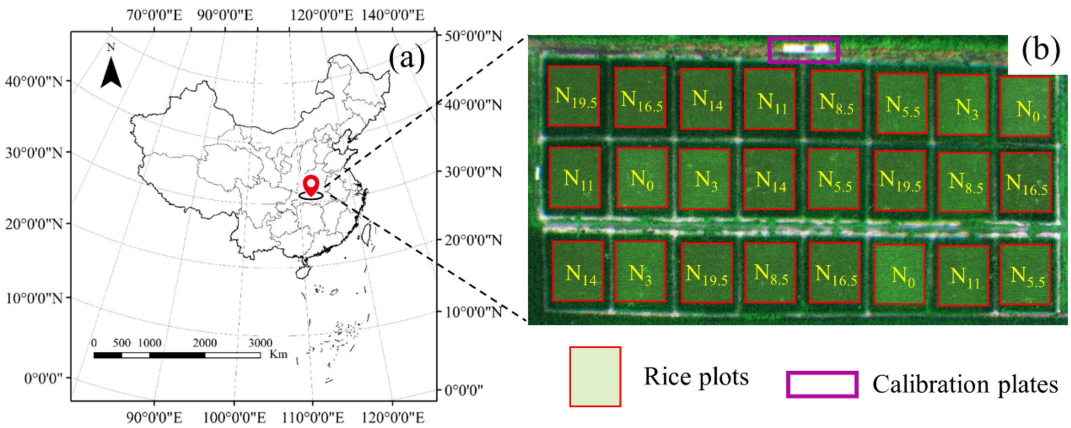

Figure 1. Study area and rice-plot settings: (**a**) experimental-area location; (**b**) nitrogen-gradient layout of rice plots.

2.2. Ground-Data Acquisition

The LAI, canopy chlorophyll content (CCC), and canopy height (CH) are significant indicators for characterizing crop yields [23,24]. Therefore, the SunScan canopy analysis system (Delta Inc., Cambridge, UK) was applied to measure the LAI of each plot. The five-point sampling method was performed at the four corners and center of each plot, and the average value was taken as the canopy LAI of each plot. At each location where the LAI was measured, three rice plants were selected, and the leaf chlorophyll was measured in the upper, middle, and lower parts of the plant using the SPAD-502 chlorophyll meter (Konica, Minolts Sensing Inc., Osaka, Japan); the mean value was recorded as the leaf chlorophyll content of each plot. The CCC is generally expressed using the product of the LAI and SPAD [25]. At each location where the LAI and SPAD were observed, three rice plants were randomly selected, and the height of the rice was measured using a millimeter ruler; the final CH was the mean value of all the readings. Rice seeds were collected by hand harvesting when the rice was fully mature. The seeds were then separated and left to dry in the sun until there were no variations in their weights. All the sun-dried seeds in each plot were weighed independently to obtain the rice yield of each plot.

2.3. Canopy Reflectance Derived from UAV Images

The UAV flights were implemented before the ground measurements. As shown in Figure 2, a multirotor UAV (S1000, SZ DJI Technology Co., Ltd., Shenzhen, China) equipped with a six-band MCA camera (Mini-MCA 6, Tetracam, Inc., Chatsworth, CA, USA) was employed to collect multispectral images of the rice at the booting (13 August 2015) and heading (29 August 2015) stages. The drone flights were conducted between 11:00 a.m. and 1:00 p.m. local time, thus ensuring minimal variation in the solar zenith angle. The multispectral camera has a center band of 490@10, 550@10, 670@10, 720@10, 800@20, or 900@20 nm. The UAV is also equipped with a three-axis gimbal to ensure that the camera is always shooting vertically downward. Four gray plates (reflectances of 6%, 12%, 24%, and 48%) were placed in the camera field of view for the radiometric calibrations to obtain the reflectance data. To prevent reflectance errors caused by solar-illumination variations, panoramic photographs of the entire study area were taken with a UAV flight altitude of 60 m and an image spatial resolution of approximately 0.03 m.

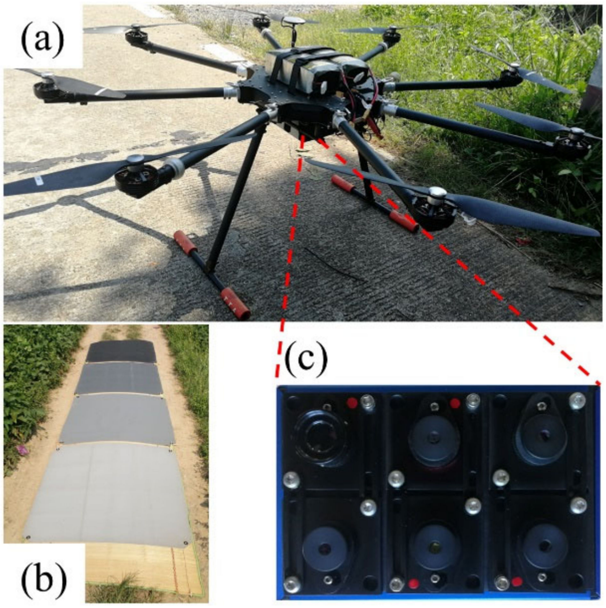

Figure 2. UAV reflectance-data-acquisition system: (**a**) UAV; (**b**) fixed reflectance grey plates for radiometric calibration; (**c**) Mini-MCA 6 multispectral camera.

The classical linear-radiometric-calibration method was utilized to transform the DN values of the multispectral images into reflectances to ensure the comparability of the data from different periods [26]. The reflectance was computed as follows:

$$R_i = DN_i \times G_i + O_i \text{ (i = 490, 550, 670, 720, 800, and 900)}, \tag{1}$$

$$\begin{pmatrix} 0.06 \\ 0.12 \\ 0.24 \\ 0.48 \end{pmatrix} = \begin{pmatrix} DN_{0.06} \\ DN_{0.12} \\ DN_{0.24} \\ DN_{0.48} \end{pmatrix} \times G_i + O_i \tag{2}$$

where R_i represents the calculated reflectance of the ith band, DN_i is the digital number of the ith band in the original multispectral images, and G_i and O_i represent the gain and offset values of the ith band, respectively.

For the 24 rice plots, we determined the maximum region of interest (ROI) suitable for each plot (equal to 10,000 pixels), and then the plot-level reflectance was the average of all the pixels in that rectangle.

2.4. VI Calculation Based on UAV Data

Several commonly available VIs obtained using combinations of visible, red-edge, and NIR bands are shown in Table 1. These VIs were selected for their good performance in crop-yield estimation and inversion of the phenotypic parameters.

Table 1. The common spectral indices selected in this paper.

Vegetation Indices	Formulas	References
Normalized Difference Vegetation Index (NDVI)	$(R_{800} - R_{670})/(R_{800} + R_{670})$	[27]
Red-Edge Chlorophyll Index ($CI_{red\ edge}$)	$R_{800}/R_{720} - 1$	[28]
Green-Edge Chlorophyll Index (CI_{green})	$R_{800}/R_{550} - 1$	[28]
Two-Band Enhanced Vegetation Index (EVI2)	$2.5(R_{800} - R_{670})/(1 + R_{800} + 2.4R_{670})$	[29]
Normalized Difference Red Edge (NDRE)	$(R_{800} - R_{720})/(R_{800} + R_{720})$	[30]
Wide-Dynamic-Range Vegetation Index (WDRVI)	$(\alpha R_{800} - \rho_{670})/(\alpha R_{800} + R_{670})$, $\alpha = 2$	[31]
MERIS Terrestrial Chlorophyll Index (MTCI)	$(R_{800} - R_{720})/(R_{720} - R_{670})$	[32]
Soil-Adjusted Vegetation Index (SAVI)	$(1 + L)(R_{800} - R_{670})/(R_{800} + R_{670} + L)$, $L = 0.5$	[33]

2.5. Tasseled Cap Transformation

TCT, which is a quadrature conversion, provides the projection of feature messages, such as the soil and vegetation in the spectral domain, into the tasseled-cap space, following the structural characteristics of the distribution of ground information in multispectral remote sensing [34]. After the TCT was performed, the spectral dimensions could be reduced, and the information was concentrated in a few feature spaces. Its defining equation is given in Equation (3):

$$y = Ax + b, \tag{3}$$

where y is the vector after the TCT; A is the unit quadrature matrix and the coefficient matrix of the TCT; x is the gray value of the image, or the apparent reflectance of the sensor; b is served as an offset vector to avoid negative values after the transformation.

When TCT was performed on six-band UAV images, the results were composed of three factors: the brightness (B), greenness (G), and third component (T). All three of these variables are intimately associated with the surface landscape. The B component represents the variation information of the reflectance, which is a weighted sum of six bands and reflects the overall brightness variation of the surface object. The G component is vertical to the B component, and it also shows the contrast between the visible band (especially the red band) and NIR band, showing the variation in the greenness of the ground vegetation, which is closely related to the ground-vegetation cover, LAI, and biomass. The T variable reflects the moisture characteristics of the soil and vegetation. Similar to calculating the plot-level reflectance, the plot-level TCT parameters were obtained by defining a rectangle (ROI).

2.6. Accuracy Evaluation Using Leave-One-Out Cross-Validation

The yield-prediction model was assessed by employing the leave-one-out cross-validation (LOO-CV) method to reduce the reliance on a single random fraction of the calibration and validation dataset [35]. In this paper, the iterative process was repeated 22 times to ensure that each piece of data was engaged in the validation (the yields of two plots were removed as a result of serious problems during harvesting). The adjusted R^2, RMSE, and MRE were selected as the final accuracy metrics [11].

3. Results

3.1. Rice-Yield Estimation using Ground Measurements at Different Stages

In this study, the rice yield at the booting and heading stages was predicted based on the plot-level LAI, CH, and CCC measured on the ground. Rice-yield data from 24 plots were compared and analyzed, two of which were removed due to obvious errors, and the remaining 22 yield data, along with the corresponding ground data, were applied for modeling analysis. The Shapiro–Wilk test was chosen to check the normality of the data before modeling the rice yield.

In Table 2, the ground measurements (yield, LAI, CH, and CCC) approximately followed a normal distribution ($p > 0.05$). Then, the phenotypic parameters and yield of the rice measured on the ground at the booting and heading stages were fitted by least-squares regression (Figure 3). It was found that the LAI was a good fit for the yield at the booting stage ($R^2 = 0.569$), but relatively poor at the heading stage ($R^2 = 0.468$).

Table 2. Data description and normality test.

Variable	Growth Stage	Min	Max	Mean	*p*-Value	CV
Yield	–	2.70	4.34	3.57	0.89	11.17%
LAI	Booting stage	2.70	6.20	4.53	0.14	15.24%
	Heading stage	2.50	6.40	4.66	0.31	17.13%
CH	Booting stage	0.70	1.03	0.91	0.08	12.36%
	Heading stage	1.03	1.25	1.16	0.06	21.66%
CCC	Booting stage	87.66	201.74	148.61	0.07	23.14%
	Heading stage	86.74	233.92	163.50	0.06	28.63%
Brightness	Booting stage	0.34	0.49	0.44	0.17	9.44%
	Heading stage	0.33	0.53	0.44	0.29	13.95%
Greenness	Booting stage	0.07	0.11	0.09	0.08	14.67%
	Heading stage	0.05	0.13	0.10	0.49	21.14%
Third Component	Booting stage	0.31	0.59	0.49	0.17	14.81%
	Heading stage	0.30	0.59	0.46	0.98	16.73%
T − G	Booting stage	0.21	0.51	0.40	0.08	20.04%
	Heading stage	0.20	0.51	0.37	0.43	22.62%
T/B	Booting stage	0.91	1.19	1.11	0.00	7.30%
	Heading stage	0.85	1.27	1.06	0.26	11.63%

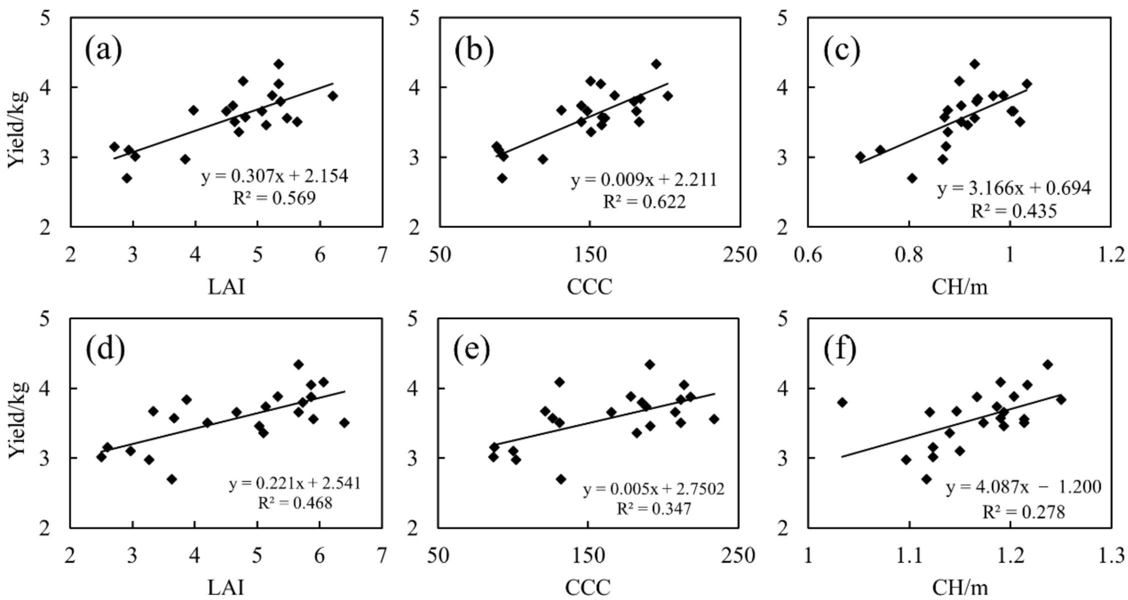

Figure 3. Fitting of ground data to yield at different growth stages: (**a**–**c**) booting stage; (**d**–**f**) heading stage.

By comparing the yield-estimation performance of the CH, LAI, and CCC, the results of a Pearson correlation analysis showed that the correlation (r) between the LAI and yield was improved by integrating SPAD data at the booting stage (Table 3), and the yield fit was significantly improved (R^2 = 0.622 vs. 0.569) (Figure 3). However, at the heading stage, the correlation decreased after combining SPAD data (R^2 = 0.468 vs. 0.347). The yield estimation with the CH was the poorest of the two periods, and especially at the heading stage. Therefore, the ground-measured LAI and SPAD data (CCC) were not suitable for predicting the yield of rice at the heading stage, but they had a good fit at the booting stage.

Table 3. Accuracy comparison of different regression models.

Growth Stage	LAI	CH	CCC (LAI × SPAD)	Brightness	Greenness	Third Component	T − G	T/B
Booting stage	0.754 **	0.659 **	0.789 **	0.585 **	−0.648 **	0.750 **	0.787 **	0.815 **
Heading stage	0.684 **	0.527 **	0.589 **	0.343 **	−0.407 **	0.739 **	0.794 **	0.702 **

** indicates that the correlation is significant at the 0.01 level (two-tailed).

3.2. Rice-Yield Estimation Using TCT Parameters

The change in rice from booting to heading is a process from nutritional to reproductive growth. Spikes basically do not appear on the surface of the rice field during the former period. In contrast, spikes progressively emerge after about two weeks. In addition to the different apparent information, there is also significant spectral diversity in rice at these two stages (Figure 4). The spectral characteristics of the rice at the booting stage were consistent with those of typical green vegetation, but they changed significantly at the heading stage. The reflectance of the rice canopy during the heading stage was significantly higher in the visible–NIR range. The appearance of rice spikes has a great influence on the spectral properties of rice.

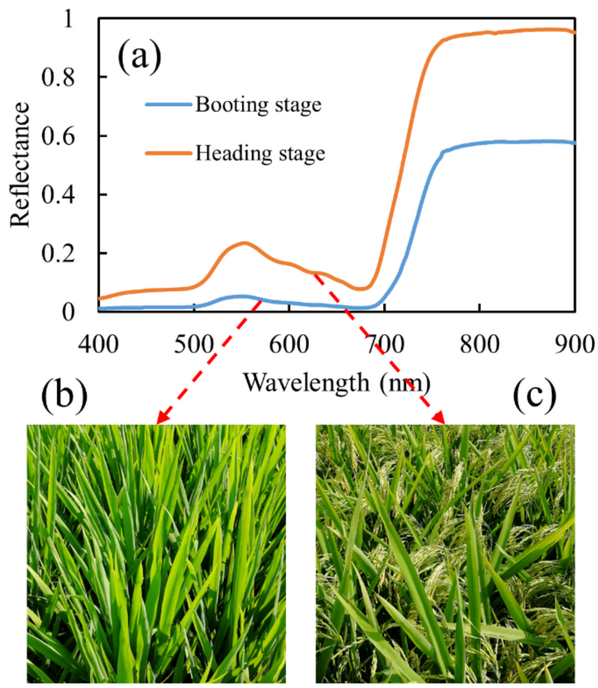

Figure 4. Spectra and field photos of rice at different stages: (**a**) spectral curves of rice at different stages; (**b**) actual view of rice at booting stage; (**c**) actual view of rice at heading stage.

Given the obvious change in the color and texture of the rice canopy caused by the appearance of panicles, paddy-field images at the booting and heading stages were obtained through a UAV equipped with a six-band Mini-MCA camera. Subsequently, the brightness, greenness, and third-component maps of the spectral-dimension reduction were retrieved by TCT (Figure 5).

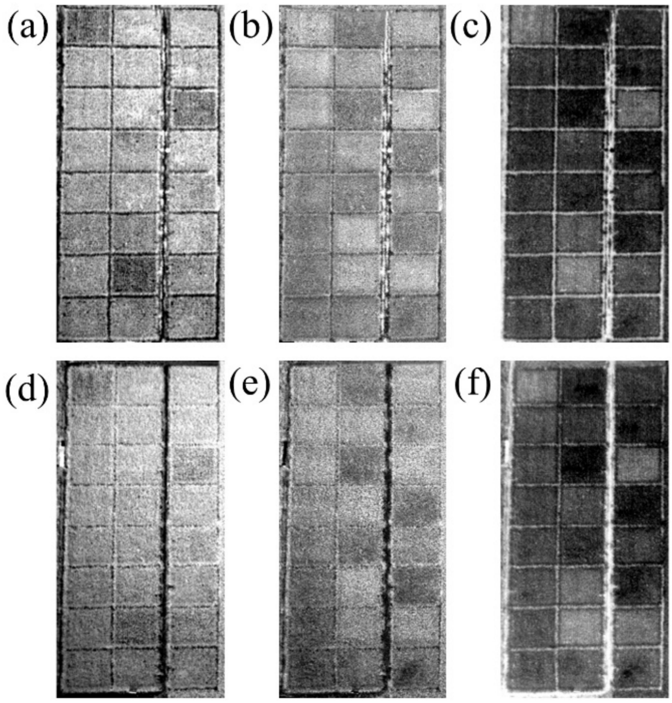

Figure 5. TCT-component images: (**a**) brightness at booting stage; (**b**) greenness at booting stage; (**c**) third component at booting stage; (**d**) brightness at heading stage; (**e**) greenness at heading stage; (**f**) third component at heading stage.

It can be noted that the TCT-component diagrams at the booting and heading stages showed a similar variation pattern. The brightness-component maps showed the overall variation in the rice reflectance throughout the experimental area, which was remarkably brighter than the greenness and third-component ones. In a single growth stage, the brightness of each plot varied with the different nitrogen-gradient conditions: the less nitrogen fertilizer applied, the darker the image. The gray distributions of the greenness and third-component images were contrary to that of the brightness-component image, which showed that the more nitrogen application applied, the darker the image. On account of the lighter color of the panicle compared with the leaf, the uneven occurrence of panicles was reflected by different greenness performances during the same growth period. For the third-component maps, the color at the booting stage was darker than that at the heading stage, reflecting the water status of the paddy fields and rice.

After completing the normality test (Table 2), a strong correlation ($r > 0.5$) was shown between the TCT parameters and rice yield during the booting period (Table 3). However, in the latter stage, the correlation between the yield and the brightness and greenness components was significantly lower. A linear fit of the yield and TCT parameters revealed a satisfactory result for the third component at both stages (R^2 values more than 0.5), but saturation was present at the booting stage (Figure 6). Meanwhile, no saturation was observed when using the brightness and greenness to predict the yield, but the performance was poor (R^2 values below 0.5 at the booting stage, and below 0.2 at the heading stage).

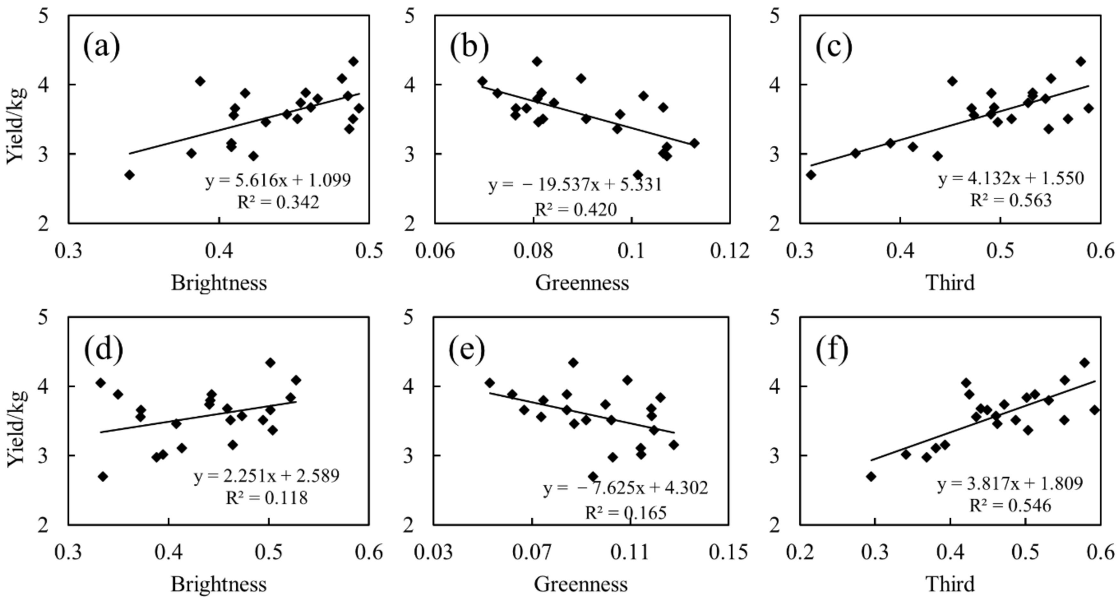

Figure 6. Fitting of TCT parameters to yield at different growth stages: (**a**–**c**) booting stage; (**d**–**f**) heading stage.

3.3. Rice-Yield Estimation Combining TCT Parameters and VIs

The correlation analysis of the yield vs. UAV-based VIs and TCT-based parameters (VI × Brightness, VI × Greenness, and VI × Third Component) was performed to compare the precision of the yield prediction at different growth stages (Figure 7). The results suggested that there was a strong correlation between the VIs and the yield at the booting stage (r > 0.7), while at the heading stage, except for the EVI2, NDRE, and SAVI, the correlation of the VIs vs. the yield decreased to some extent, and especially the CI_{green} vs. yield. Multiplied by the TCT parameters, some of the VIs had a stronger correlation with the yield, which was more obvious at the heading stage. At the heading stage, the brightness improved the correlation between the $CI_{red\ edge}$, CI_{green}, NDRE, WDRVI, and MTCI and the yield. The greenness only improved the correlation of the $CI_{red\ edge}$ and CI_{green} vs. the yield, and the third component basically improved the correlation between all the listed VIs and the yield. Based on the correlation analysis, the yield estimation of the rice was carried out on 22 samples at the booting and heading stages: (1) yield vs. Vis; (2) yield vs. VI × Brightness; (3) yield vs. VI × Greenness; (4) yield vs. VI × Third Component. The adjusted R^2 and RMSE were used to evaluate the performance of the yield prediction.

The yield-estimation results of the rice at the booting stage are shown in Table 4. The best-estimated yield parameter in the VIs was the WDRVI, with an adjusted R^2 of 0.634. The prediction results of the VI × Brightness and VI × Third Component were improved to a certain degree. In contrast, the performance of the VI × Greenness was worse. After combining the TCT parameters, the optimal yield-estimation variable was the CI_{green}. Several models with the best fitting effect were selected for analysis (shown in Figure 8). Except for the CI_{green} × Brightness, the other models (WDRVI, CI_{green} × Greenness, CI_{green} × Third Component) were saturated with different degrees, of which the WDRVI was the most obvious one.

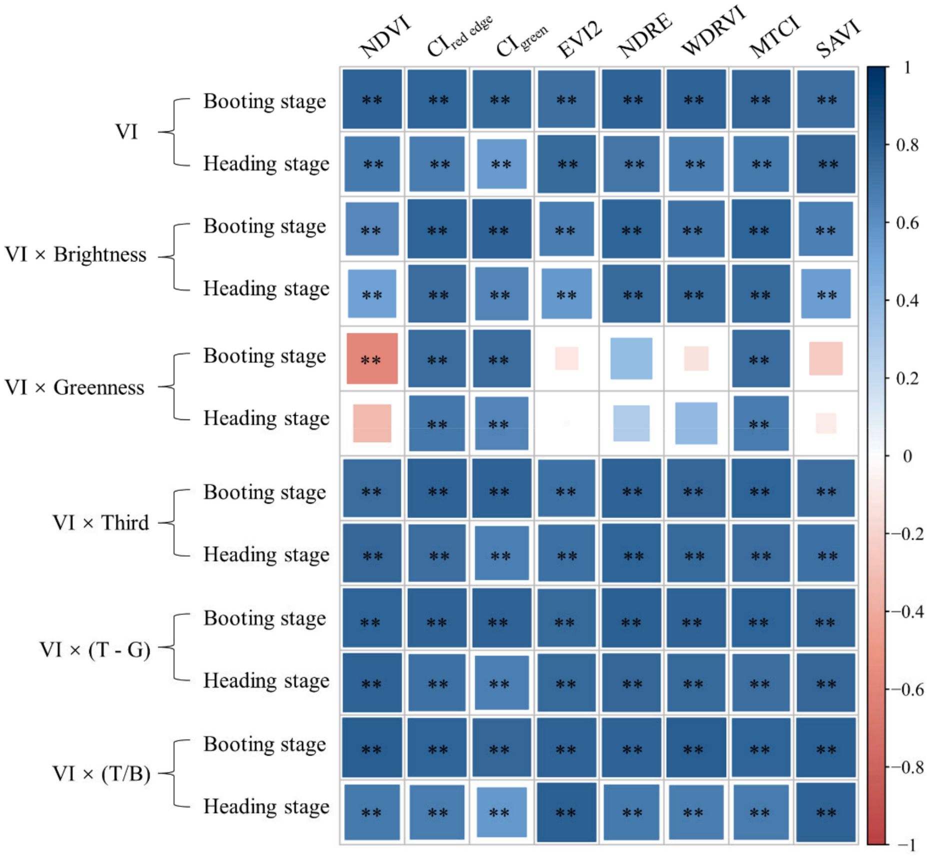

Figure 7. Correlation coefficients between parameters of VI and TCT combinations and yield (** indicates that the correlation is significant at the 0.01 level).

Table 4. Yield-estimation models incorporating TCT parameters and VIs at the booting stage.

Evaluating Indicators	Parameters	NDVI	$CI_{red\ edge}$	CI_{green}	EVI2	NDRE	WDRVI	MTCI	SAVI
Adjusted R^2	VI	0.628	0.614	0.591	0.553	0.624	0.634	0.606	0.558
	VI × Brightness	0.406	0.622	0.638	0.449	0.614	0.532	0.620	0.441
	VI × Greenness	0.345	0.562	0.568	0.016	0.152	0.019	0.565	0.062
	VI × Third Component	0.575	0.624	0.637	0.545	0.633	0.604	0.622	0.550
	VI × (T − G)	0.622	0.623	0.636	0.584	0.639	0.631	0.621	0.592
	VI × (T/B)	0.665	0.620	0.603	0.635	0.637	0.662	0.614	0.645
RMSE	VI	0.254	0.265	0.273	0.283	0.261	0.254	0.268	0.281
	VI × Brightness	0.334	0.264	0.257	0.321	0.265	0.290	0.265	0.323
	VI × Greenness	0.342	0.281	0.278	0.426	0.407	0.428	0.280	0.411
	VI × Third Component	0.277	0.264	0.258	0.289	0.259	0.266	0.265	0.286
	VI × (T − G)	0.262	0.265	0.259	0.276	0.257	0.258	0.266	0.273
	VI × (T/B)	0.245	0.263	0.269	0.256	0.256	0.245	0.266	0.252

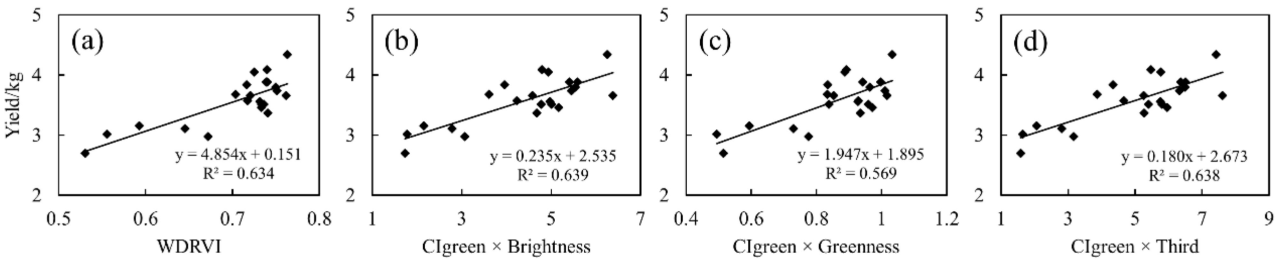

Figure 8. Well-performing yield-estimation models incorporating TCT parameters and VIs at the booting stage.

The rice-yield-prediction results at the heading stage are shown in Table 5. Compared with the booting stage, the parameters with the best fitting performance changed, indicating that the sensitivity of the VIs to the yield varied after the emergence of panicles. The VI with the best fitting performance in this period was the SAVI (adjusted R^2 = 0.600). Multiplied by the TCT parameters, the estimated result of the VI × Third Component had a certain degree of improvement. However, the fitting effects of the VI × Brightness and VI × Greenness were worse. Similarly, the models with good fitting effects were selected for analysis (Figure 9). Except for the SAVI, the other models (WDRVI × Brightness, $CI_{red\ edge}$ × Greenness, NDRE × Third Component) did not show significant saturation. Therefore, the most appropriate parameter to predict the rice yield at the heading stage was the NDRE × Third Component (Adjusted R^2 = 0.612, RMSE = 0.272).

Table 5. Yield-estimation models incorporating TCT parameters and VIs at the heading stage.

Evaluating Indicators	Parameters	NDVI	$CI_{red\ edge}$	CI_{green}	EVI2	NDRE	WDRVI	MTCI	SAVI
Adjusted R^2	VI	0.477	0.472	0.305	0.585	0.506	0.460	0.485	0.600
	VI × Brightness	0.273	0.574	0.409	0.324	0.582	0.583	0.580	0.302
	VI × Greenness	0.105	0.497	0.409	0.003	0.088	0.158	0.466	0.010
	VI × Third Component	0.597	0.555	0.436	0.533	0.612	0.589	0.567	0.542
	VI × (T − G)	0.634	0.546	0.436	0.583	0.604	0.581	0.558	0.595
	VI × (T/B)	0.484	0.459	0.314	0.640	0.488	0.454	0.472	0.633
RMSE	VI	0.308	0.310	0.352	0.276	0.299	0.312	0.307	0.269
	VI × Brightness	0.379	0.287	0.329	0.363	0.281	0.279	0.285	0.369
	VI × Greenness	0.396	0.306	0.329	0.432	0.436	0.417	0.317	0.426
	VI × Third Component	0.275	0.292	0.320	0.298	0.272	0.277	0.289	0.295
	VI × (T − G)	0.264	0.295	0.320	0.283	0.275	0.280	0.291	0.279
	VI × (T/B)	0.305	0.313	0.349	0.258	0.304	0.314	0.310	0.260

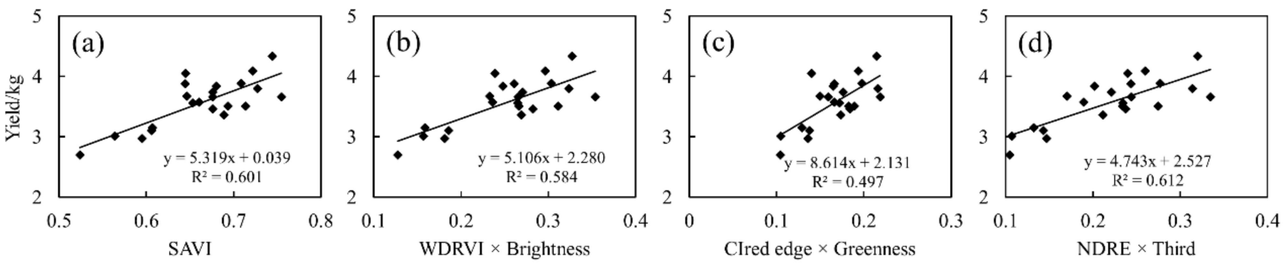

Figure 9. Well-performing yield-estimation models incorporating TCT parameters and VIs at the heading stage.

The TCT parameters were transformed to further improve the accuracy of the rice-yield estimation and reduce the model saturation. On the one hand, Figure 6 reveals that the third component was the best fit for the yield at the booting and heading stages, while the brightness and greenness components were poorly fitted for the yield. On the other hand, the yield was positively correlated with the brightness and third component, and negatively correlated with the greenness component. In addition, the fitting model of the third component and the yield had an obvious saturation phenomenon at the booting stage, which did not exist in the other components. Therefore, two new parameters of the difference between the third component and greenness (T − G) and the quotient of the third component and brightness (T/B) were constructed to fuse the various features of the TCT parameters. The correlation between the new parameters and the yield was significantly enhanced at the booting and heading stages (Figure 7). The rice-yield-prediction results of the VIs incorporating the new TCT parameters are shown in Tables 4 and 5. At the booting stage, the VIs incorporating T – G and T/B had high yield-estimation accuracy (RMSE < 0.276 in the VI × (T − G) model, and RMSE < 0.269 in the VI × (T/B) model). Figure 10 shows the yield-simulation models of the VIs incorporating the newly constructed parameters, and there was high accuracy in all the models at both periods (R^2 values are more than 0.6). Nevertheless, all the models at the booting stage had obvious saturation, but none at the heading stage. This indicated that the VIs combining the information of the brightness, greenness, and wetness had good suitability for estimating the rice yield at the heading stage: high accuracy and low saturation.

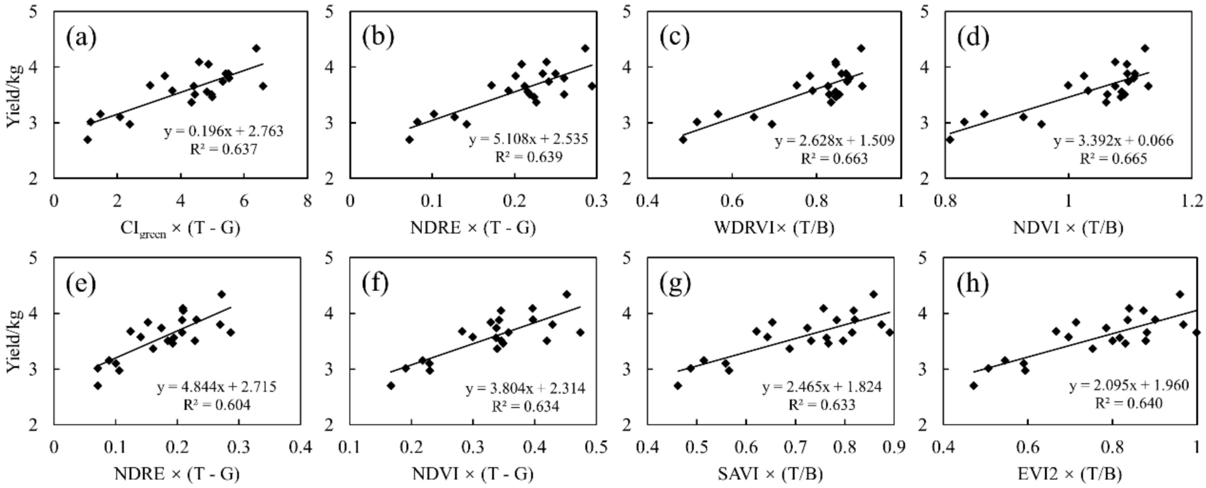

Figure 10. Well-performing yield-estimation models incorporating TCT combination parameters and VIs at different stages: (**a**–**d**) booting stage; (**e**–**h**) heading stage.

At length, the LOO-CV method was used to verify the model of the rice-yield estimation at the heading stage, and the results are shown in Figure 11. The model estimation errors of the NDRE × (T − G), NDVI × (T − G), SAVI × (T/B), and EVI2 × (T/B) were less than 7%.

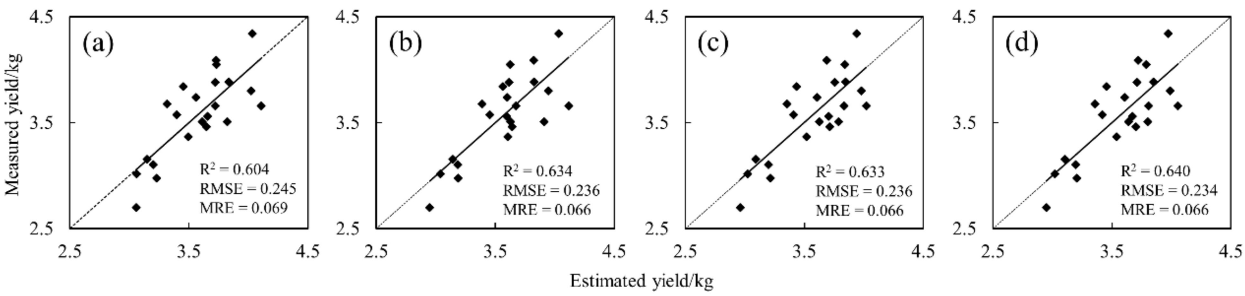

Figure 11. Accuracy-assessment results of the VI × (T − G) and VI × (T/B) models at the heading stage: (**a**) NDRE × (T − G); (**b**) NDVI × (T − G); (**c**) SAVI × (T/B); (**d**) EVI2 × (T/B).

4. Discussion

The main purpose of this paper is to improve the accuracy of rice-yield estimation and reduce the saturation of the models by using the information on the brightness, greenness, and wetness obtained from TCT and combining the UAV-based VIs. The results demonstrated that the VIs incorporating the TCT parameters had good potential to solve these two problems. In crop-yield-estimation studies, an increasing number of parameters have been used in conjunction with VIs. For example, variables such as the canopy texture [36], canopy height [24,37], canopy coverage [24], and temperature [38] are frequently fused by machine-learning methods to improve the crop-yield-estimation accuracy [39]. However, this approach is too complex, and the models have limited robustness. In this paper, we combine the advantages of the VIs and TCT parameters in a simple way through a quadratic operation, which is both easy and has significant accuracy improvement.

The reason for selecting the research period of rice in this paper was that the morphology was not completely stable at the tillering stage and jointing stage, and the leaves and stems changed greatly in a short time. Furthermore, the filling stage and ripening stage were close to the harvesting stage, and thus the yield data obtained was of little value. At the booting and heading stages, the rice gradually completed the transition from vegetative growth to reproductive growth. At the booting stage, there were almost no panicles in the rice canopy, while at the heading stage, with the continuous growth of the rice, the panicles gradually appeared until they covered the whole canopy. Other than that, there was no significant change in this stage relative to the booting stage (Figure 4b,c). Wang et al. proposed that the single-growth-stage model (RNDVI) $_{(880, 712)}$ at the booting stage was most suitable for the yield estimation of rice, with an R^2 of 0.75 [18]. Duan et al. pointed out a new method integrating UAV-based VIs and abundance information retrieved from spectral mixture analysis to improve the yield-estimation precision of rice at the heading stage [11]. Zhang et al. put forward that the estimation of the grain yield during the early to mid-growth stages was significant for the initial diagnosis of rice and the quantitative regulation of topdressing [40]. Kawamura et al. demonstrated that the booting stage might be the optimum time for in-season rice-grain assessment [41]. Zhou et al. held that the booting stage was determined as the optimal period for grain-yield estimation using VIs at a single stage for both digital images and multispectral images [19]. Therefore, based on the principle of prediction possibility and time advance, the optimum growth period for rice-yield simulation was determined to be the booting stage, but the heading stage also had great potential for high-precision estimation.

We tried to compare the effects of different data sources on the rice-yield estimation in various stages by collecting the ground data (CH, LAI, and CCC) and UAV remote-sensing images at the booting and heading stages. Peng et al. remotely predicted the yield of oilseed rape based on LAI estimation, with good performance [42]. Hence, the rice yield was first estimated by LAI data. The results showed that the predictive ability of the LAI at the booting stage was significantly better than that at the heading stage (R^2 = 0.569 vs. 0.468) (Figure 3). Liu et al. utilized the LAI integrated with SPAD (LAI × SPAD) data to demonstrate the potential of estimating rice yields [25]. The LAI × SPAD data and rice yield in this paper were also used for regression analysis, and the results showed that they significantly enhanced the ability to predict the rice yield at the booting stage, with an obvious improvement compared with the LAI (Figure 3). However, at the heading stage, the CCC reduced the prediction ability of the rice yield, even worse than the simulation ability of the LAI, which indicated that the appearance of panicles at the heading stage weakened the predicted potential of the LAI and SPAD. Liu et al. also deemed that the CCC completely derived from the green leaves of rice had a good correlation with the yield [25]. Consequently, it was reasonable to speculate that the main reason for the decline in the yield-estimation ability at the heading stage was the emergence of panicles because the SunScan canopy analysis system was used in the LAI measurement. According to its measuring principle, panicles and stems were also a part of the LAI output information, which was probably unrelated to the yield estimation.

With the improvements in RS technology, more crop-canopy images with different spatial scales can be obtained, including multispectral and hyperspectral images [17,43]. VIs calculated by the combination of different bands is one of the most used methods for yield estimation [44]. The eight plot-level VIs (NDVI, $CI_{red\ edge}$, CI_{green}, EVI2, NDRE, WDRVI, MTCI, and SAVI) were extracted from the multispectral images at the booting and heading stages of rice. Then, the VIs and yield data were fitted by the least-squares method. The results showed a good performance at the booting stage, with a minimum RMSE of the WDRVI of 0.254 (Table 4). The simulation results of the other VIs listed at this stage were also satisfactory (RMSE < 0.283). However, there was a most prominent problem of vulnerability to saturation in the VI-based simulation models. The apparent saturation phenomenon exhibited that most of the WDRVI values were concentrated around 0.75 (Figure 8). At the heading stage, the ability of the VIs to predict the yield decreased significantly. Except for the SAVI and EVI2, the simulation accuracies of the rest of the VIs were very poor (RMSE > 0.3) (Table 5). The CI_{green} of the fitting model, in particular, had an adjustment R^2 of 0.305. The calculation of the CI_{green} combined with the reflectance of the green band, and the appearance of panicles, largely reflected the green characteristics of the rice, thus affecting the correlation with the yield. According to the simulation results of the SAVI, the saturation phenomenon was still very distinct (Figure 9). In general, whether it was the booting stage or heading stage, the rice yield simulated by the VIs was inevitably saturated.

The appearance of panicles at the heading stage will lead to changes in the rice-canopy color and other characteristics, which, in turn, have a direct impact on the canopy reflectance. Therefore, the TCT method was used to extract the brightness, greenness, and wetness information of the rice at the booting and heading stages to improve the yield-estimation accuracy and eliminate the saturation. It was found from the TCT-component maps (Figure 5) that the brightness image at the booting stage was darker than that at the heading stage, while the greenness and wetness images at the heading stage were darker than those at the booting stage. This is because the reflectance of the rice canopy at the heading stage was significantly higher than that at the booting stage, and the brightness map was a direct mirror of the reflectance. Due to the appearance of panicles, the greenness of the rice-canopy leaves at the heading stage was replaced by the light color of some of the panicles, resulting in a decrease in the greenness. According to the water requirement of rice, it is necessary to irrigate enough water at the booting stage, and at the heading stage, the water in the paddy fields should be drained off irregularly. Thereby, the wetness of rice fields at the heading stage would decrease. A correlation analysis and regression analysis were performed on the TCT parameters and yield data—(Table 3 and Figure 6). The results showed that the brightness and greenness had poor simulation effects on the yield, while the wetness had a better effect. However, the saturation appeared in the simulation model of the wetness at the booting stage, but it did not exist at the heading stage. In a word, the direct use of the brightness, greenness, and wetness information was not enough to accurately simulate the rice yield.

Combining the different advantages of the VIs and TCT parameters to simulate the rice yield (high precision and low saturation), the method of VIs multiplied by TCT components was employed in this paper. Although some of the parameters were well simulated, the simulation accuracy of the VI × Greenness models at the booting stage, the VI × Brightness, and the VI × Greenness models at the heading stage were lower than those of the VI models. Moreover, there were different degrees of saturation in the fitting models at the booting stage, but none at the heading stage. In combination with the characteristics of different TCT parameters (correlation and saturation), VI × (T − G) and VI × (T/B) were established to estimate the yield of rice at different stages. The models at the booting stage were still saturated, while the simulation models at the heading stage showed high precision with no obvious saturation, and estimation errors below 7%. Consequently, the VIs, which combined the information of the brightness, greenness, and wetness, were suitable for estimating the rice yield at the heading stage.

In this paper, we developed a new approach to estimating rice yields at the booting and heading stages using the integration of VIs and the brightness, greenness, and wetness information retrieved from UAV multispectral images. This method is simple and feasible, but it has crucial reference significance for the yield estimation of rice and similar crops. Moreover, the theoretical and technical support was provided for the crop-yield estimation with evident changes in the canopy over time. In the future, we will further set up more dense nitrogen-fertilizer gradients to explore the best nitrogen-application amount for rice. In terms of the LAI measurement, some new instruments (for example, the LI-3100C table leaf-area meter, LI-COR, USA) will be used to avoid the impact of the panicles and stems on the output of the LAI, and more realistic LAI data will be obtained to improve and validate the accuracy of rice-yield estimations by ground-measurement data. Concurrently, this method will be applied to satellite data and other crops to enable the rapid, nondestructive, and high-precision estimation of crop yields over larger areas.

5. Conclusions

In this study, we developed a technique to improve the estimation of rice yields at the booting and heading stages using UAV-based VIs and TCT-based parameter data. The ground-measurement data could only be used to predict the rice yield at the booting stage, and the prediction ability was lost at the heading stage due to the uneven occurrence of panicles. The UAV-based VIs had similar prediction performances to the ground measurements. Although the accuracy was high at the booting stage, the yield-estimation models were seriously saturated. To improve the prediction accuracy and reduce the saturation of the models, TCT was applied to eliminate the effect of the panicle emergence at the heading stage on the yield estimation. The TCT-component images at the booting and heading stages of the paddy fields were produced based on the six-band UAV images, including the brightness, greenness, and third component (wetness). It was more accurate to use the integration of the plot-level VIs and TCT-parameter information to estimate the rice yield than using VIs alone. Among all the parameters, the $CI_{green} \times (T - G)$, NDRE $\times$ (T − G), WDRVI $\times$ (T/B), and NDVI $\times$ (T/B) at the booting stage, and NDRE $\times$ (T − G), NDVI $\times$ (T − G), SAVI $\times$ (T/B), and EVI2 $\times$ (T/B) at the heading stage, were the most accurate indicators for the rice-yield estimation under different nitrogen-fertilizer treatments, with estimation errors below 7%. The VIs, which combined the brightness, greenness, and third component, were more suitable for estimating the rice yield at the heading stage, with their advantages of high accuracy and low saturation. This paper can provide theoretical and technical support for crop-phenotype-parameter extraction and precision agriculture.

Author Contributions: Conceptualization, S.L. and X.J.; methodology, S.L.; software, W.J.; validation, S.F.; writing—original draft preparation, S.L.; writing—review and editing, S.L., K.Y. and Y.L.; funding acquisition, S.F. All authors have read and agreed to the published version of the manuscript.

Funding: This research was funded by the National Key Research and Development Project (2016YFD0101105), the Phenomics Research and New Variety Creation of Hybrid Rice Based on UAV Remote Sensing (2020BBB058), and the National High-tech Research and Development Program (863 Program) (2013AA102401).

Institutional Review Board Statement: Not applicable.

Informed Consent Statement: Not applicable.

Data Availability Statement: Not applicable.

Conflicts of Interest: The authors declare no conflict of interest.

References

1. Zhu, Y.G.; Williams, P.N.; Meharg, A.A. Exposure to inorganic arsenic from rice: A global health issue? *Environ. Pollut.* **2008**, *154*, 169–171. [CrossRef]
2. Zhang, J.T.; Feng, L.P.; Zou, H.P.; Liu, D.L. Using ORYZA2000 to model cold rice yield response to climate change in the Heilongjiang province, China. *Crop J.* **2015**, *3*, 317–327. [CrossRef]
3. Yang, G.J.; Liu, J.G.; Zhao, C.J.; Li, Z.H.; Huang, Y.B.; Yu, H.Y.; Xu, B.; Yang, X.D.; Zhu, D.M.; Zhang, X.Y.; et al. Unmanned aerial vehicle remote sensing for field-based crop phenotyping: Current status and perspectives. *Front. Plant Sci.* **2017**, *8*, 26. [CrossRef]
4. Zhang, J.T.; Tian, H.Q.; Yang, J.; Pan, S.F. Improving representation of crop growth and yield in the dynamic land ecosystem model and its application to China. *J. Adv. Model. Earth Syst.* **2018**, *10*, 1680–1707. [CrossRef]
5. Luo, S.; He, Y.B.; Li, Q.; Jiao, W.H.; Zhu, Y.Q.; Zhao, X.H. Nondestructive estimation of potato yield using relative variables derived from multi-period LAI and hyperspectral data based on weighted growth stage. *Plant Methods* **2020**, *16*, 14. [CrossRef]
6. Palosuo, T.; Kersebaum, K.C.; Angulo, C.; Hlavinka, P.; Moriondo, M.; Olesen, J.E.; Patil, R.H.; Ruget, F.; Rumbaur, C.; Takac, J.; et al. Simulation of winter wheat yield and its variability in different climates of Europe: A comparison of eight crop growth models. *Eur. J. Agron.* **2011**, *35*, 103–114. [CrossRef]
7. Liu, N.F.; Budkewitsch, P.; Treitz, P. Examining spectral reflectance features related to Arctic percent vegetation cover: Implications for hyperspectral remote sensing of Arctic tundra. *Remote Sens. Environ.* **2017**, *192*, 58–72. [CrossRef]
8. Vilfan, N.; van der Tol, C.; Muller, O.; Rascher, U.; Verhoef, W. Fluspect-B: A model for leaf fluorescence, reflectance and transmittance spectra. *Remote Sens. Environ.* **2016**, *186*, 596–615. [CrossRef]
9. Kross, A.; McNairn, H.; Lapen, D.; Sunohara, M.; Champagne, C. Assessment of RapidEye vegetation indices for estimation of leaf area index and biomass in corn and soybean crops. *Int. J. Appl. Earth Obs. Geoinf.* **2015**, *34*, 235–248. [CrossRef]

10. Moharana, S.; Dutta, S. Spatial variability of chlorophyll and nitrogen content of rice from hyperspectral imagery. *ISPRS-J. Photogramm. Remote Sens.* **2016**, *122*, 17–29. [CrossRef]
11. Duan, B.; Fang, S.H.; Zhu, R.S.; Wu, X.T.; Wang, S.Q.; Gong, Y.; Peng, Y. Remote estimation of rice yield with unmanned aerial vehicle (UAV) data and spectral mixture analysis. *Front. Plant Sci.* **2019**, *10*, 14. [CrossRef] [PubMed]
12. Lobell, D.B.; Azzari, G.; Burke, M.; Gourlay, S.; Jin, Z.; Kilic, T.; Murray, S. Eyes in the sky, boots on the ground: Assessing satellite- and ground-based approaches to crop yield measurement and analysis. *Am. J. Agr. Econ.* **2020**, *102*, 202–219. [CrossRef]
13. Schwalbert, R.A.; Amado, T.J.C.; Nieto, L.; Varela, S.; Corassa, G.M.; Horbe, T.A.N.; Rice, C.W.; Peralta, N.R.; Ciampitti, I.A. Forecasting maize yield at field scale based on high-resolution satellite imagery. *Biosyst. Eng.* **2018**, *171*, 179–192. [CrossRef]
14. Cao, H.T.; Gu, X.F.; Sun, Y.; Gao, H.L.; Tao, Z.; Shi, S.Y. Comparing, validating and improving the performance of reflectance obtention method for UAV-Remote sensing. *Int. J. Appl. Earth Obs. Geoinf.* **2021**, *102*, 15. [CrossRef]
15. Aslan, M.F.; Durdu, A.; Sabanci, K.; Ropelewska, E.; Gueltekin, S.S. A comprehensive survey of the recent studies with UAV for precision agriculture in open fields and greenhouses. *Appl. Sci.* **2022**, *12*, 29. [CrossRef]
16. Liu, S.S.; Li, L.T.; Gao, W.H.; Zhang, Y.K.; Liu, Y.N.; Wang, S.Q.; Lu, J.W. Diagnosis of nitrogen status in winter oilseed rape (*Brassica napus* L.) using in-situ hyperspectral data and unmanned aerial vehicle (UAV) multispectral images. *Comput. Electron. Agric.* **2018**, *151*, 185–195. [CrossRef]
17. Deng, L.; Mao, Z.H.; Li, X.J.; Hu, Z.W.; Duan, F.Z.; Yan, Y.N. UAV-based multispectral remote sensing for precision agriculture: A comparison between different cameras. *ISPRS-J. Photogramm. Remote Sens.* **2018**, *146*, 124–136. [CrossRef]
18. Wang, F.L.; Wang, F.M.; Zhang, Y.; Hu, J.H.; Huang, J.F.; Xie, J.K. Rice yield estimation using parcel-level relative spectra variables from UAV-based hyperspectral imagery. *Front. Plant Sci.* **2019**, *10*, 12. [CrossRef]
19. Zhou, X.; Zheng, H.B.; Xu, X.Q.; He, J.Y.; Ge, X.K.; Yao, X.; Cheng, T.; Zhu, Y.; Cao, W.X.; Tian, Y.C. Predicting grain yield in rice using multi-temporal vegetation indices from UAV-based multispectral and digital imagery. *ISPRS-J. Photogramm. Remote Sens.* **2017**, *130*, 246–255. [CrossRef]
20. Duan, B.; Fang, S.H.; Gong, Y.; Peng, Y.; Wu, X.T.; Zhu, R.S. Remote estimation of grain yield based on UAV data in different rice cultivars under contrasting climatic zone. *Field Crop. Res.* **2021**, *267*, 11. [CrossRef]
21. Joshi, P.P.; Wynne, R.H.; Thomas, V.A. Cloud detection algorithm using SVM with SWIR2 and tasseled cap applied to Landsat 8. *Int. J. Appl. Earth Obs. Geoinf.* **2019**, *82*, 10. [CrossRef]
22. Mostafiz, C.; Chang, N.B. Tasseled cap transformation for assessing hurricane landfall impact on a coastal watershed. *Int. J. Appl. Earth Obs. Geoinf.* **2018**, *73*, 736–745. [CrossRef]
23. Wang, Z.L.; Chen, J.X.; Zhang, J.W.; Fan, Y.F.; Cheng, Y.J.; Wang, B.B.; Wu, X.L.; Tan, X.M.; Tan, T.T.; Li, S.L.; et al. Predicting grain yield and protein content using canopy reflectance in maize grown under different water and nitrogen levels. *Field Crop. Res.* **2021**, *260*, 15. [CrossRef]
24. Wan, L.; Cen, H.Y.; Zhu, J.P.; Zhang, J.F.; Zhu, Y.M.; Sun, D.W.; Du, X.Y.; Zhai, L.; Weng, H.Y.; Li, Y.J.; et al. Grain yield prediction of rice using multi-temporal UAV-based RGB and multispectral images and model transfer–A case study of small farmlands in the South of China. *Agric. For. Meteorol.* **2020**, *291*, 15. [CrossRef]
25. Liu, X.J.; Zhang, K.; Zhang, Z.Y.; Cao, Q.; Lv, Z.F.; Yuan, Z.F.; Tian, Y.C.; Cao, W.X.; Zhu, Y. Canopy chlorophyll density based index for estimating nitrogen status and predicting grain yield in rice. *Front. Plant Sci.* **2017**, *8*, 12. [CrossRef]
26. Smith, G.M.; Milton, E.J. The use of the empirical line method to calibrate remotely sensed data to reflectance. *Int. J. Remote Sens.* **1999**, *20*, 2653–2662. [CrossRef]
27. Tucker, C.J. Red and photographic infrared linear combinations for monitoring vegetation. *Remote Sens. Environ.* **1979**, *8*, 127–150. [CrossRef]
28. Gitelson, A.A.; Gritz, Y.; Merzlyak, M.N. Relationships between leaf chlorophyll content and spectral reflectance and algorithms for non-destructive chlorophyll assessment in higher plant leaves. *J. Plant Physiol.* **2003**, *160*, 271–282. [CrossRef]
29. Jiang, Z.Y.; Huete, A.R.; Didan, K.; Miura, T. Development of a two-band enhanced vegetation index without a blue band. *Remote Sens. Environ.* **2008**, *112*, 3833–3845. [CrossRef]
30. Gitelson, A.; Merzlyak, M.N. Quantitative estimation of chlorophyll-a using reflectance spectra: Experiments with autumn chestnut and maple leaves. *J. Photochem. Photobiol. B-Biol.* **1994**, *22*, 247–252. [CrossRef]
31. Gitelson, A.A. Wide dynamic range vegetation index for remote quantification of biophysical characteristics of vegetation. *J. Plant Physiol.* **2004**, *161*, 165–173. [CrossRef] [PubMed]
32. Dash, J.; Curran, P.J. The MERIS terrestrial chlorophyll index. *Int. J. Remote Sens.* **2004**, *25*, 5403–5413. [CrossRef]
33. Huete, A.R. A soil-adjusted vegetation index (SAVI). *Remote Sens. Environ.* **1988**, *25*, 295–309. [CrossRef]
34. Crist, E.P.; Cicone, R.C. A physically-based transformation of thematic mapper data—The TM tasseled cap. *IEEE Trans. Geosci. Remote Sensing* **1984**, *22*, 256–263. [CrossRef]
35. Wong, T.T. Performance evaluation of classification algorithms by k-fold and leave-one-out cross validation. *Pattern Recognit.* **2015**, *48*, 2839–2846. [CrossRef]
36. Ma, Y.R.; Ma, L.L.; Zhang, Q.; Huang, C.P.; Yi, X.; Chen, X.Y.; Hou, T.Y.; Lv, X.; Zhang, Z. Cotton yield estimation based on vegetation indices and texture features derived from RGB image. *Front. Plant Sci.* **2022**, *13*, 17. [CrossRef]
37. Li, B.; Xu, X.M.; Zhang, L.; Han, J.W.; Bian, C.S.; Li, G.C.; Liu, J.G.; Jin, L.P. Above-ground biomass estimation and yield prediction in potato by using UAV-based RGB and hyperspectral imaging. *ISPRS-J. Photogramm. Remote Sens.* **2020**, *162*, 161–172. [CrossRef]

38. Fei, S.P.; Hassan, M.A.; Xiao, Y.G.; Su, X.; Chen, Z.; Cheng, Q.; Duan, F.Y.; Chen, R.Q.; Ma, Y.T. UAV-based multi-sensor data fusion and machine learning algorithm for yield prediction in wheat. *Precis. Agric.* **2022**, *23*, 26. [CrossRef]
39. Ashapure, A.; Jung, J.H.; Chang, A.J.; Oh, S.; Yeom, J.; Maeda, M.; Maeda, A.; Dube, N.; Landivar, J.; Hague, S.; et al. Developing a machine learning based cotton yield estimation framework using multi-temporal UAS data. *ISPRS-J. Photogramm. Remote Sens.* **2020**, *169*, 180–194. [CrossRef]
40. Zhang, K.; Ge, X.K.; Shen, P.C.; Li, W.Y.; Liu, X.J.; Cao, Q.; Zhu, Y.; Cao, W.X.; Tian, Y.C. Predicting rice grain yield based on dynamic changes in vegetation indexes during early to mid-growth stages. *Remote Sens.* **2019**, *11*, 24. [CrossRef]
41. Kawamura, K.; Ikeura, H.; Phongchanmaixay, S.; Khanthavong, P. Canopy hyperspectral sensing of paddy fields at the booting stage and PLS regression can assess grain yield. *Remote Sens.* **2018**, *10*, 15. [CrossRef]
42. Peng, Y.; Zhu, T.E.; Li, Y.C.; Dai, C.; Fang, S.H.; Gong, Y.; Wu, X.T.; Zhu, R.S.; Liu, K. Remote prediction of yield based on LAI estimation in oilseed rape under different planting methods and nitrogen fertilizer applications. *Agric. For. Meteorol.* **2019**, *271*, 116–125. [CrossRef]
43. Feng, W.; Guo, B.B.; Zhang, H.Y.; He, L.; Zhang, Y.S.; Wang, Y.H.; Zhu, Y.J.; Guo, T.C. Remote estimation of above ground nitrogen uptake during vegetative growth in winter wheat using hyperspectral red-edge ratio data. *Field Crop. Res.* **2015**, *180*, 197–206. [CrossRef]
44. Hatfield, J.L.; Gitelson, A.A.; Schepers, J.S.; Walthall, C.L. Application of spectral remote sensing for agronomic decisions. *Agron. J.* **2008**, *100*, S117–S131. [CrossRef]